

The multi-millennial Antarctic commitment to future sea-level rise

N. R. Golledge^{1,2}, D. E. Kowalewski³, T. R. Naish^{1,2}, R. H. Levy², C. J. Fogwill⁴ & E. G. W. Gasson⁵

Atmospheric warming is projected to increase global mean surface temperatures by 0.3 to 4.8 degrees Celsius above pre-industrial values by the end of this century¹. If anthropogenic emissions continue unchecked, the warming increase may reach 8–10 degrees Celsius by 2300 (ref. 2). The contribution that large ice sheets will make to sea-level rise under such warming scenarios is difficult to quantify because the equilibrium-response timescale of ice sheets is longer than those of the atmosphere or ocean. Here we use a coupled ice-sheet/ice-shelf model to show that if atmospheric warming exceeds 1.5 to 2 degrees Celsius above present, collapse of the major Antarctic ice shelves triggers a centennial- to millennial-scale response of the Antarctic ice sheet in which enhanced viscous flow produces a long-term commitment (an unstoppable contribution) to sea-level rise. Our simulations represent the response of the present-day Antarctic ice-sheet system to the oceanic and climatic changes of four representative concentration pathways (RCPs) from the Fifth Assessment Report of the Intergovernmental Panel on Climate Change³. We find that substantial Antarctic ice loss can be prevented only by limiting greenhouse gas emissions to RCP 2.6 levels. Higher-emissions scenarios lead to ice loss from Antarctic that will raise sea level by 0.6–3 metres by the year 2300. Our results imply that greenhouse gas emissions in the next few decades will strongly influence the long-term contribution of the Antarctic ice sheet to global sea level.

Ice sheets lose mass and contribute to global mean sea level (GMSL) by surface and basal melting, and by dynamic thinning^{4,5}. Melting typically occurs at the ice surface if air temperatures are above zero, and at the ice base either where grounded ice is at the pressure melting point, or where ice is afloat in the ocean⁶. Owing to the exchange of heat between ice and adjacent water or air, changes in environmental temperature may cause changes in melt rate. Dynamic ice loss involves large-scale adjustment of part of an ice sheet to a change in the force balance that determines the ice flow speed (for example, loss of a buttressing ice shelf⁶). There may be a delay in the dynamic ice-sheet response because although perturbations may be transmitted rapidly through ice shelves, the grounded ice sheet takes time to relax to a new steady state. Understanding which environmental changes lead to an immediate, and which to a lagged, ice-sheet response is important in predicting the timescale and transient evolution of the perturbed ice-sheet contribution to GMSL, as well as the total contribution that anthropogenic greenhouse-gas emissions will ultimately commit the planet to.

In Antarctica, peripheral ice shelves restrain the flow of grounded ice⁷ and are sensitive to warming air and ocean temperatures^{8–10}. Observations show that 67% to 98% of ocean warming since 2006 occurred in the Southern Ocean¹¹, with a similar multidecadal trend in the heat content of circum-Antarctic waters¹². Air temperatures across Antarctica, especially in West Antarctica, have risen on average 0.6 °C in the past 50 years¹³. Precipitation has also increased, but there remains a net acceleration of mass loss from Antarctica¹⁴ that continues to contribute to rising sea levels¹⁵. Recent studies indicate

that parts of West Antarctica may already be undergoing irreversible retreat^{16,17}, and several studies^{18,19} have focused on quantifying the resultant Antarctic contribution to GMSL by 2100. Predicting the multi-centennial-scale to millennial-scale commitments implied by future climate scenarios²⁰ and palaeoclimate equilibrium ice-sheet reconstructions for high-carbon-dioxide (CO₂) conditions^{21,22} has received less attention, however.

Some studies have investigated long-term commitments to sea-level rise under global warming scenarios using statistical relationships between past temperatures and global sea levels^{20,23}. Here we present numerical simulations of the Antarctic ice-sheet/ice-shelf system response to environmental changes predicted by four RCPs of the Fifth Assessment Report of the Intergovernmental Panel on Climate Change³ (Extended Data Fig. 1; Extended Data Table 1), which we extend to 5000 CE to capture the multi-millennial response (see ‘Methods’ and Extended Data Fig. 2). We use the Parallel Ice-Sheet Model, an open-source, three-dimensional, thermodynamic, coupled ice-sheet/ice-shelf model^{24,25}, and run simulations at spatial resolutions of 10 km and 20 km. Our method employs two different grounding-line parameterizations to quantify the likely range of ice-sheet responses. One implementation uses sub-grid interpolation of basal melting at grounding lines²⁶ whereas the other does not²⁷ (see Methods). Because the former tends to accelerate grounding-line retreat in coarse-resolution models such as ours we refer to sea-level contributions from these simulations as ‘high’ and those that do not include the sub-grid basal melt interpolation as ‘low’. Other schemes may produce even higher or lower values, however.

The most immediate response to predicted climate changes in all but our RCP 2.6 experiment is a reduction in extent of the major ice shelves (Ross, Filchner-Ronne and Amery) within 100–300 years (Fig. 1). Reduced ice-shelf buttressing leads to increased discharge and flow acceleration that promotes grounding-line recession in areas where marine-based ice sheets occupy deep basins (such as West Antarctica; Fig. 1e, h, k). In our ‘high’ simulations, prolonged warming also leads to substantial loss of ice in East Antarctica, particularly in the Wilkes subglacial basin, at the margin of the Aurora subglacial basin, and in the southern and eastern Weddell Sea embayment (pale blue shading and blue lines in Fig. 1f, i and l). Under RCP 8.5 the range of sea-level contributions predicted by our ‘low’ and ‘high’ simulations respectively is 0.1–0.39 m by 2100, increasing to 1.6–2.96 m by 2300 and 5.2–9.31 m by 5000 CE (Figs 1j–l and 2a). Rates of sea-level rise are 5.5–15 mm per year by 2300 under RCP 8.5 conditions, but even under the lesser forcings of RCP 4.5 and RCP 6 reach 3–5 mm per year by 2300 (Figs 1e, h and 2a). These simulations show that systemic lags delay the fastest rates of ice-sheet loss by decades to centuries following the onset of initial forcing (Fig. 2a).

The initial ice-sheet/ice-shelf responses are important, but are relatively modest compared to the responses triggered now that will take place (committed changes) over subsequent millennia (Fig. 1c, f, i, l). In our experiments we see clear correspondence between the magnitude of

¹Antarctic Research Centre, Victoria University of Wellington, Wellington 6140, New Zealand. ²GNS Science, Avalon, Lower Hutt 5011, New Zealand. ³Department of Earth, Environment, and Physics, Worcester State University, Worcester, Massachusetts 01602, USA. ⁴Climate Change Research Centre, University of New South Wales, Sydney, New South Wales 2052, Australia. ⁵Climate System Research Center, University of Massachusetts Amherst, Amherst, Massachusetts 01003, USA.



Figure 1 | Modelled ice-sheet evolution under Antarctic-specific RCP-based warming scenarios. Emissions-forced climate warming to 2100 CE (a, d, g, j) and 2300 CE (b, e, h, k) results in initial sea-level contributions from Antarctica that are only a small proportion of the total sea-level commitment by 5000 CE (c, f, i, l). Magnitudes and rates of sea-level contributions are shown for each panel. Leading values and those in parentheses relate to 'low' and 'high' scenarios respectively. Ice extent for 'low' simulations is shown in

white; blue lines show grounding-line locations for 'high' simulations. Pale blue shading shows grounded ice lost in 'high' simulations but present in the 'low' scenario. Note the increasing divergence between 'high' and 'low' beyond 2300 CE. Grey texturing indicates areas of relatively faster-flowing ice. WAIS, West Antarctic Ice Sheet; EAIS, East Antarctic Ice Sheet; FRIS, Filchner–Ronne Ice Shelf.

a multi-millennial environmental perturbation, the steady-state area of fringing ice shelves, and the long-term ice-sheet contribution to GMSL (Fig. 2b). Specifically, we observe a sharp decline in near-equilibrium ice-shelf extent when atmospheric and oceanic temperatures are maintained 1.2 °C and 0.3 °C respectively above present. Almost all floating ice is lost if equilibrium air and ocean temperatures increase by more than 2 °C and 0.5 °C above present, respectively. These ice shelf 'thresholds' (defined here as an abrupt reduction in area to 50% of present) also occur during centennial-scale adjustment of the ice sheet to new equilibria, but happen at different temperatures (Fig. 2b). We infer therefore that short-lived (decadal-scale) environmental perturbations may mimic the longer-term responses if the former are of a large enough magnitude.

To isolate the causes of lags in the simulated ice-sheet/ice-shelf system and identify mechanisms by which the system responds to

atmospheric and oceanic forcings, we ran 32 sensitivity experiments (using the full grounding-line scheme) that isolated changes in air temperature, precipitation and sea surface temperature (ΔT_{air} , ΔP_{eff} and ΔSST) and simplified the time-varying RCP forcings (Fig. 3a, b). Each simplified forcing experiment comprised a perturbation-free interval from 0–2000 CE and a linear increase in T_{air} , P_{eff} or SST from 2000 CE to either 2100 CE or 2300 CE, after which the forcing was maintained unchanged for the remainder of the run (up to 5000 CE). This simplification was designed to clearly identify modelled ice-sheet response to each applied forcing.

Figure 3 illustrates the response of the modelled ice sheet when forced with each of the three environmental forcings (ΔT_{air} , ΔP_{eff} and ΔSST) in isolation, and when all three are combined, under the warmest of the simplified RCP scenarios (RCP 8.5) and using the full grounding-line scheme. Figure 3c and d shows that the timing of

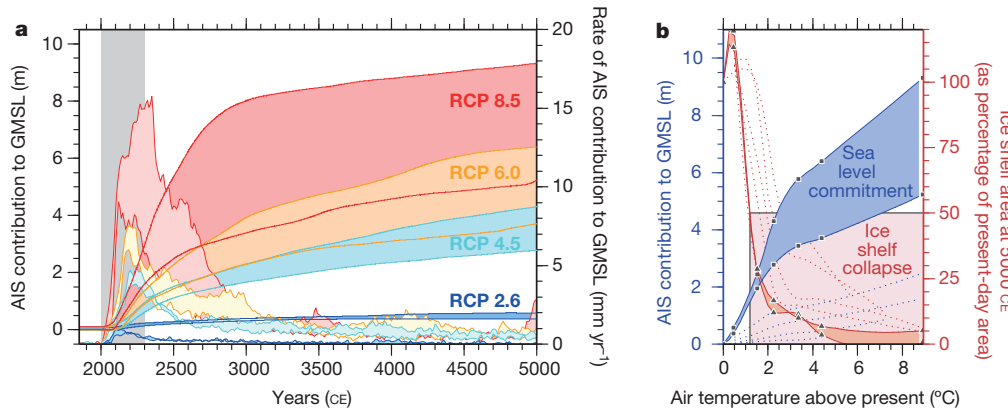


Figure 2 | Antarctic Ice Sheet (AIS) contribution to GMSL. **a**, Predicted sea-level contribution from the Antarctic ice sheet for ‘high’ and ‘low’ simulations (coloured lines) under each of the four RCP scenarios (darker shading), based on coeval climatic and oceanic perturbations. The forced response (grey shading) represents 20% to 36% of the committed response by 5000 CE. Lighter shading between coloured lines shows rates of sea-level-equivalent ice loss for each scenario. **b**, Long-term sea-level commitment as a function of atmospheric warming (blue shading with squares). Intermediate response

ice-sheet response to a warming atmosphere is similar for both 2100 and 2300 scenarios with rate-of-change maxima at 2244–2316 CE, several centuries from the start of the perturbation. In contrast, peak ice-volume responses to precipitation changes manifest only 11–41 years after the end of each forcing period. A warming ocean results in a 26-year peak-response lag when forced to 2100 CE, but there is no lag when forced to 2300 CE. In summary, precipitation changes produce rapid sea-level-equivalent ice-volume changes because of their direct and immediate addition of mass to the ice sheet. Warming of the atmosphere leads to an immediate loss of mass through surface melt in some areas (especially West Antarctica), but the effect is small and generally a warming atmosphere produces a lagged volumetric response that requires 200–300 years from the initial forcing to reach a maximum. Thermal changes in the ocean bring about rapid ice-sheet responses that, using the full grounding-line scheme, are far greater in magnitude than those arising from atmospheric forcings alone, and

curves for the ‘low’ simulations are shown as dotted lines. Red shading with triangles shows the relationship between ice-shelf area and atmospheric warming for the near-equilibrium response and for intermediate stages (dotted lines). All curves in **b** are based on data from the four RCP scenario simulations, further constrained by two additional experiments whose maximum air temperature forcings are 1.5 °C and 3.35 °C. Pink shading defines the temperature range within which an ice shelf extent that is less than 50% of the present extent is simulated.

exhibit little to no lag. Despite these differences, all forcings lead to committed responses that manifest as rates of change that are higher than those of the initial conditions for thousands of years after the forcing period (Extended Data Fig. 5).

The mechanisms responsible for the differing responses seen in Fig. 3 can be inferred from time-series of glaciological changes (Fig. 4). Rising air temperatures increase the total volume of temperate ice (ice that is close to melting point; brown line in Fig. 4a), which, because it is softer and more easily deformed, leads to an increase in the non-sliding, or ‘creep’, component of domain-averaged grounded-ice velocity (Fig. 4c) (the domain is the model grid). Together with an accompanying increase in sliding velocity, atmospheric thermal forcing leads to gradual thinning of parts of the ice sheet and a consequent reduction in the domain-averaged gravitational driving stress (Fig. 4b). Although the warming perturbation in each simulation is applied only from 2000–2300 CE, softening of the ice and non-sliding

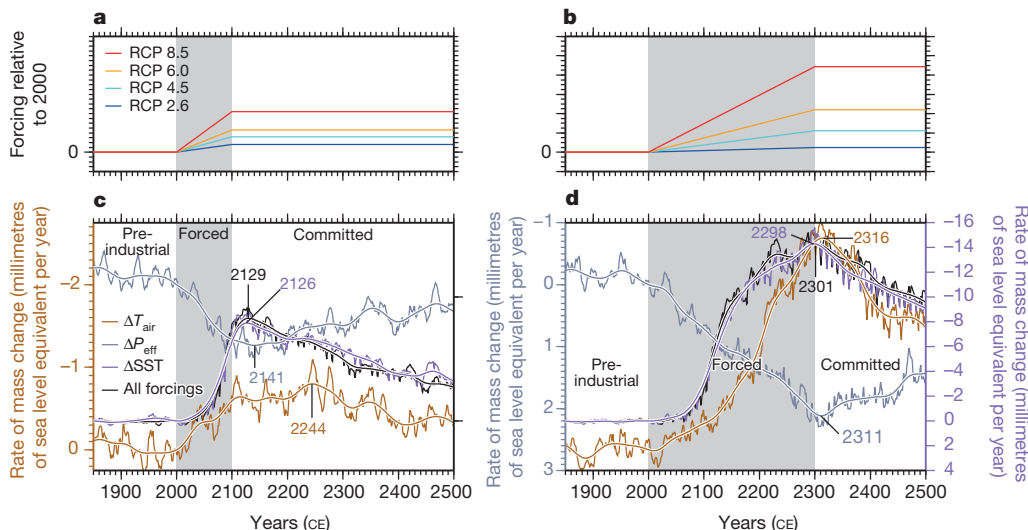


Figure 3 | Response of modelled Antarctic ice sheet to simplified environmental forcings. **a, b**, The relative magnitudes of air temperature ΔT_{air} , effective precipitation ΔP_{eff} and sea surface temperature ΔSST forcings for simplified RCP scenarios based on likely Antarctic values at 2100 CE (**a**) and 2300 CE (**b**). **c, d**, Trends in sea-level-equivalent ice mass rate-of-change that arise using the full grounding-line scheme and when forced with changes in ΔT_{air} , ΔP_{eff} , ΔSST , or the combination of these forcings, based on simplified

RCP 8.5 scenarios for 2100 (**c**) and 2300 (**d**). Note the different y -axis scales. Coloured numbers in **c** and **d** identify peak rates of change in the 100-year Gaussian-smoothed response curves. Data are shown relative to zero at 2000 CE. Grey shading shows periods of applied forcing. Absolute changes in ice-sheet volume and area (rather than rates of change) to 5000 CE are shown in Extended Data Fig. 4.

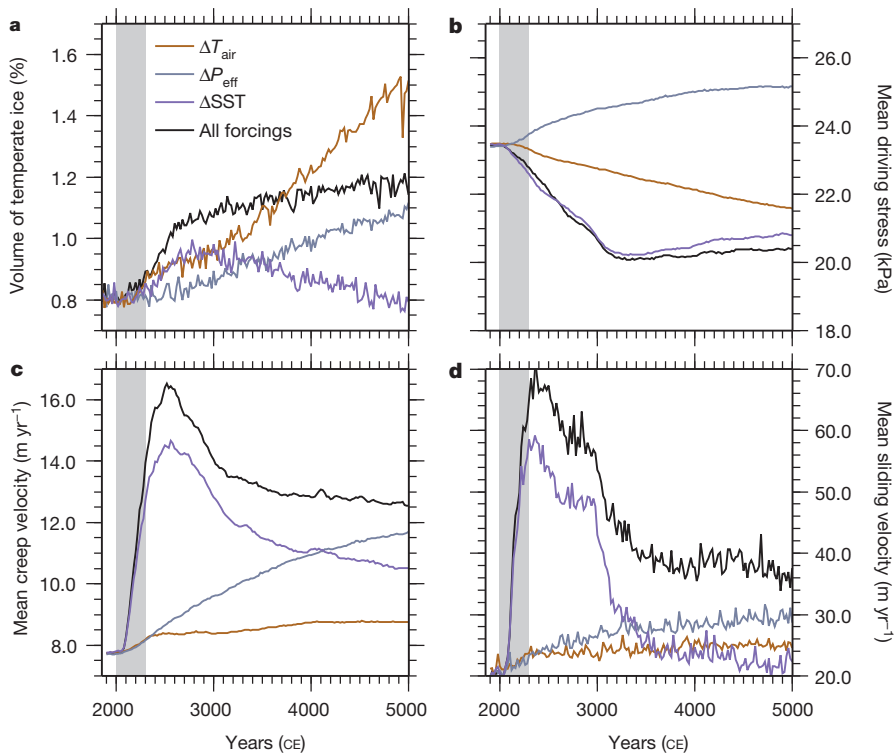


Figure 4 | Glaciological changes taking place under single-parameter environmental perturbations. **a**, Domain-wide changes in the volume of temperate ice. **b**, Mean driving stress of grounded ice. **c**, **d**, Averages of the non-sliding (**c**) and sliding (**d**) components of grounded ice velocity. All curves are from the simplified RCP 8.5, 2300 CE, ‘high’ simulations (Fig. 3b). Grey shading denotes period of applied forcing.

ice velocity continue to increase throughout the experiment, perhaps as a consequence of internal feedbacks such as strain heating, which would encourage faster ice flow and advection of ‘warmer’ ice deeper into the ice sheet, as proposed previously²⁸. Increased precipitation, even when applied in the absence of atmospheric warming, leads to an increase in the volume of temperate ice (grey line in Fig. 4a), probably because highest precipitation occurs in coastal areas under relatively warm conditions. Increased accumulation results in a greater domain-averaged ice thickness, which in turn increases the mean driving stress (Fig. 4b). Non-sliding ice velocities increase markedly throughout the simulation (Fig. 4c), probably as a consequence of increased ice thickness and increased driving stress²⁹.

By reducing the volume of floating ice shelves through basal melting, increased ocean temperatures lead to an overall reduction in the proportion of temperate ice in the domain (purple line in Fig. 4a). Thinning of grounded ice in response to loss of buttressing ice shelves means that the domain-averaged driving stress is reduced (Fig. 4b), but both sliding and non-sliding components of ice velocity increase abruptly during the forcing period (Fig. 4c, d). The acceleration of sliding velocities probably reflects the reduction in back-pressure exerted by the rapidly diminishing ice shelves⁷, whereas deformation rates probably increase as a consequence of internal strain heating and frictional heating at the bed due to faster flow²⁸. Flow acceleration then declines from about 3000 CE, perhaps because grounding lines occupy stable slopes once the major deep basins have been vacated, illustrating that the dynamic response to a loss of buttressing is transient and may be topographically controlled.

In summary, oceanic warming produces a much greater and more rapid ice-sheet response than atmospheric warming, but the rate of ice volume change forced by the warming of the ocean peaks and declines more quickly than the rate of change forced by atmospheric warming, which is more gradual and sustained for longer (Extended Data Fig. 5). Whereas ocean-forced perturbations produce the greatest ice-sheet contribution to sea level on centennial timescales (approximately five times that produced by increased air temperature alone when the full grounding-line scheme is used), contributions due to atmospheric warming become increasingly important over multi-millennial periods. The loss of buttressing ice shelves, the consequent increase in

sliding velocity of grounded ice and thinning at the ice-sheet margin, combined with the thermal softening effect of warming atmospheric temperatures that increases the creep-rate of grounded ice, all govern the long-term response of the ice sheet and lag times of this system. Ice-sheet response to external forcing is therefore mediated both by ice-stream dynamics and the timescale of adjustment of viscous flow (‘creep’) of grounded ice, which together produce a commitment to sea level rise that persists for multiple millennia.

Unless anthropogenic greenhouse-gas emissions are reduced to half of 1990 levels by 2050, global mean annual surface temperatures are likely to exceed 2 °C above pre-industrial values by 2100 (ref. 30). This aggressive mitigation scenario corresponds to RCP 2.6, which both our ‘low’ and ‘high’ simulations show is the only ocean-climate regime in which the long-term Antarctic contribution to GMSL does not exceed 1 m (Fig. 2a). Under all other RCP scenarios the future commitment to a rise in sea level from Antarctica is substantial. This commitment arises because the collapse of buttressing ice shelves leads to a dynamic ice-sheet response that greatly increases grounded ice discharge for hundreds to thousands of years into the future, even if greenhouse-gas emissions are reduced and temperatures stabilize (Supplementary Videos 1 and 2). The results presented here and elsewhere⁸ suggest that ice-shelf stability is vulnerable to a critical temperature threshold. In our experiments, we find that prolonged ocean warming of 0.5 °C above present, together with atmospheric warming of 2 °C, ultimately leads to the loss of 80% to 85% of all floating ice in Antarctica.

Online Content Methods, along with any additional Extended Data display items and Source Data, are available in the online version of the paper; references unique to these sections appear only in the online paper.

Received 13 April; accepted 3 September 2015.

1. Meinshausen, M. et al. The RCP greenhouse gas concentrations and their extensions from 1765 to 2300. *Clim. Change* **109**, 213–241 (2011).
2. Rogelj, J., Meinshausen, M. & Knutti, R. Global warming under old and new scenarios using IPCC climate sensitivity range estimates. *Nature Clim. Change* **2**, 248–253 (2012).
3. Collins, M. et al. in *Climate Change 2013: The Physical Science Basis. Contribution of Working Group I to the Fifth Assessment Report of the Intergovernmental Panel on Climate Change* (eds Stocker, T. et al.) 1029–1136 (Cambridge Univ. Press, 2013).

4. Pritchard, H. D. et al. Antarctic ice-sheet loss driven by basal melting of ice shelves. *Nature* **484**, 502–505 (2012).
5. Wouters, B. et al. Dynamic thinning of glaciers on the Southern Antarctic Peninsula. *Science* **348**, 899–903 (2015).
6. Joughin, I. & Alley, R. B. Stability of the West Antarctic ice sheet in a warming world. *Nature Geosci.* **4**, 506–513 (2011).
7. Scambos, T. A., Bohlander, J. A., Shuman, C. A. & Skvarca, P. Glacier acceleration and thinning after ice shelf collapse in the Larsen B embayment, Antarctica. *Geophys. Res. Lett.* **31**, L18402 (2004).
8. Vaughan, D. G. & Doake, C. S. M. Recent atmospheric warming and retreat of ice shelves on the Antarctic Peninsula. *Nature* **379**, 328–331 (1996).
9. Liu, Y. et al. Ocean-driven thinning enhances iceberg calving and retreat of Antarctic ice shelves. *Proc. Natl Acad. Sci. USA* **112**, 3263–3268 (2015).
10. Paolo, F. S., Fricker, H. A. & Padman, L. Volume loss from Antarctic ice shelves is accelerating. *Science* **348**, 327–331 (2015).
11. Roemmich, D. et al. Unabated planetary warming and its ocean structure since 2006. *Nature Clim. Change* **5**, 240–245 (2015).
12. Schmidtko, S., Heywood, K. J., Thompson, A. F. & Aoki, S. Multidecadal warming of Antarctic waters. *Science* **346**, 1227–1231 (2014).
13. Steig, E. J. et al. Warming of the Antarctic ice-sheet surface since the 1957 International Geophysical Year. *Nature* **457**, 459–462 (2009).
14. Harig, C. & Simons, F. J. Accelerated West Antarctic ice mass loss continues to outpace East Antarctic gains. *Earth Planet. Sci. Lett.* **415**, 134–141 (2015).
15. Hay, C. C., Morrow, E., Kopp, R. E. & Mitrovica, J. X. Probabilistic reanalysis of twentieth-century sea-level rise. *Nature* **517**, 481–484 (2015).
16. Joughin, I., Smith, B. E. & Medley, B. Marine ice sheet collapse potentially under way for the Thwaites Glacier basin, West Antarctica. *Science* **344**, 735–738 (2014).
17. Rignot, E., Mouginot, J., Morlighem, M., Seroussi, H. & Scheuchl, B. Widespread, rapid grounding line retreat of Pine Island, Thwaites, Smith, and Kohler glaciers, West Antarctica, from 1992 to 2011. *Geophys. Res. Lett.* **41**, 3502–3509 (2014).
18. Bindschadler, R. et al. Ice-sheet model sensitivities to environmental forcing and their use in projecting future sea-level (The SeaRISE Project). *J. Glaciol.* **59**, 195–224 (2013).
19. Levermann, A. et al. Projecting Antarctic ice discharge using response functions from SeaRISE ice-sheet models. *Earth Syst. Dyn.* **5**, 271–293 (2014).
20. Levermann, A. et al. The multimillennial sea-level commitment of global warming. *Proc. Natl Acad. Sci. USA* **110**, 13745–13750 (2013).
21. Naish, T. et al. Obliquity-paced Pliocene West Antarctic ice sheet oscillations. *Nature* **458**, 322–328 (2009).
22. Pollard, D. & DeConto, R. M. Modelling West Antarctic ice sheet growth and collapse through the past five million years. *Nature* **458**, 329–332 (2009).
23. Schaeffer, M., Hare, W., Rahmstorf, S. & Vermeer, M. Long-term sea-level rise implied by 1.5 °C and 2 °C warming levels. *Nature Clim. Change* **2**, 867–870 (2012).
24. Bueler, E. & Brown, J. Shallow shelf approximation as a “sliding law” in a thermomechanically coupled ice sheet model. *J. Geophys. Res.* **114**, F03008 (2009).
25. Winckelmann, R. et al. The Potsdam Parallel Ice Sheet Model (PISM-PIK)—Part 1: Model description. *Cryosphere* **5**, 715–726 (2010).
26. Feldmann, J. & Levermann, A. Interaction of marine ice-sheet instabilities in two drainage basins: simple scaling of geometry and transition time. *Cryosphere* **9**, 631–645 (2015).
27. Feldmann, J., Albrecht, T., Khroulev, C., Pattyn, F. & Levermann, A. Resolution-dependent performance of grounding line motion in a shallow model compared to a full-Stokes model according to the MISMIP3d intercomparison. *J. Glaciol.* **60**, 353–360 (2014).
28. Clarke, G. K., Nitsan, U. & Paterson, W. Strain heating and creep instability in glaciers and ice sheets. *Rev. Geophys.* **15**, 235–247 (1977).
29. Winckelmann, R., Levermann, A., Frieler, K. & Martin, M. Increased future ice discharge from Antarctica owing to higher snowfall. *Nature* **492**, 239–242 (2012).
30. Meinshausen, M. et al. Greenhouse-gas emission targets for limiting global warming to 2 °C. *Nature* **458**, 1158–1162 (2009).

Supplementary Information is available in the online version of the paper.

Acknowledgements We thank the CMIP community for making their data openly available, and J. Lenaerts for providing present-day surface mass balance data. We are also grateful to K. Buckley (Victoria University high-performance computing cluster), C. Khroulev, T. Albrecht and the Parallel Ice Sheet Model groups at the University of Alaska, Fairbanks, and the Potsdam Institute for Climate Impact Research. This work was funded by contract VUW1203 of the Royal Society of New Zealand’s Marsden Fund, with support from the Antarctic Research Centre, Victoria University of Wellington, ANDRILL, GNS Science (NZ Ministry of Business Innovation and Employment contract C05X1001), National Science Foundation grant ANT-1043712, and the Australian Research Council (ARC). J. Renwick and D. Zwart provided comments that improved the manuscript.

Author Contributions N.R.G. devised and carried out the ice-sheet modelling experiments and D.E.K. undertook climate model simulations to produce the present-day ocean temperature field. All authors contributed to the development of ideas and writing of the manuscript.

Author Information Reprints and permissions information is available at www.nature.com/reprints. The authors declare no competing financial interests. Readers are welcome to comment on the online version of the paper. Correspondence and requests for materials should be addressed to N.R.G. (nicholas.golledge@vuw.ac.nz).

METHODS

The ice-sheet model. Continental-scale studies such as ours are currently unable to reproduce the level of detail that catchment-scale studies resolve^{31,32}, but they nonetheless offer useful insights that arise from their wider geographic coverage. For our suite of experiments we use the Parallel Ice Sheet Model (PISM) version 0.6.3, an open-source, three-dimensional, thermodynamic, coupled ice-sheet/ice-shelf model. The model combines equations of the shallow-ice and shallow-shelf approximations for grounded ice, and uses the shallow-shelf approximation for floating ice²⁴. Superposing the shallow-ice and shallow-shelf velocity solutions allows basal sliding to be simulated according to the ‘dragging shelf’ approach²⁴, and enables a consistent treatment of stress regime across the grounded-ice to floating-ice transition²⁵. Ice streams develop naturally as a consequence of plastic failure of saturated basal till³³, depending on the thermal regime and volume of water at the ice-sheet bed. The amount of water that saturates basal till varies spatially according to the enthalpy field, but is limited in our implementation so that no more than a 2-m thickness of saturated substrate accumulates. This subglacial hydrology model does not conserve water, in the sense that any additional water above the imposed maximum thickness is permanently lost. Till pore water pressure is defined as a maximum of 0.8 times the ice-overburden pressure (Extended Data Table 2). The effective pressure calculated from meltwater thickness and ice overburden, together with the spatially varying till friction angle, is then used to calculate the yield strength of basal substrate, which will vary in time and space as basal meltwater volumes change. The till friction angle is prescribed heuristically at the start of the run, and follows a simple elevation dependence such that deeper basins that are likely to hold deformable sediments are assigned lower values than higher areas, which are more likely to be rock. In our simulations, we choose values of 10° for areas below ~1,000 m, and 30° for areas above 200 m. Intermediate values are linearly interpolated between these extrema. For computational tractability we employed a resolution of 10 km for our ‘realistic’ RCP simulations, and a resolution of 20 km for our ‘simplified’ RCP experiments, where the focus lies on investigating the differences between results of different environmental forcings, rather than simply the magnitudes or rates of ice retreat.

Migration of the grounding line is facilitated through a sub-grid scheme that calculates one-sided derivatives for surface slope above and below the grounding line, and interpolates basal shear stress in x , y according to the spatial gradient between adjacent grounded and floating cells²⁷. Additionally, we impose reduced basal traction in the first cell upstream of the grounding line, in which the basal resistance calculated from the computed pore water content is replaced by a basal drag value that assumes saturation of the basal substrate. In this way, basal shear stress gradients across the grounding line are reduced and a more dynamic margin is facilitated, in line with current theory^{34,35}. For our ‘high’ simulations we also use a sub-grid scheme that interpolates sub-shelf melt rates at the grounding line^{26,27}.

Climate data (air temperature, precipitation) are used as inputs to a positive degree-day scheme that calculates surface mass balance. We use degree-day factors of 3 mm K⁻¹ per day and 8 mm K⁻¹ per day for snow and ice respectively. Random white noise is included in the calculation to mimic natural variability. An elevation dependence of -0.008 Km^{-1} is applied to air temperatures in areas where the surface elevation changes. Basal melting of floating ice is calculated thermodynamically using a three-component temperature–salinity scheme³⁶. This scheme yields the highest melt rates adjacent to ice-sheet grounding lines and lower melt rates, or accretion, closer to the central sectors of modelled ice shelves. Calving of floating ice is calculated from horizontal strain rates^{37,38} with an additional heuristically based minimum thickness condition applied. PISM incorporates a sophisticated bed deformation model in which changes in ice load effect both elastic and viscous responses in the underlying bedrock³⁹. Time-dependent variations in relative sea level therefore arise in our simulations from isostatic adjustment according to the flexural rigidity of the crust and the viscosity-dependent lateral displacement of the mantle. Self-gravitational sea-level effects that arise from changes in ice-sheet mass are not included, however, and consequently our model may not capture the potentially stabilizing feedback of a local lowering of sea level⁴⁰. This effect, which becomes more important over multi-centennial timescales, is typically smaller than isostatic effects, which are included in our simulations, so the influence on our short-term predictions should be minimal. Because we also do not account for self-gravitational rises in local sea level, which may occur in response to loss of ice from distal sectors of the ice sheet, we may in fact underestimate margin retreat in some areas.

Climate and ocean inputs.

Present-day conditions. To define the initial conditions for our experimental ensemble, we employ spatially distributed data sets of annual mean air temperatures, annual precipitation totals, and circum-Antarctic sea surface temperatures from a selection of recent observational and model-based compilations.

The most recent and widely used map of Antarctic surface mass balance derives from regional atmospheric climate modelling using RACMO2.1/ANT45. These

data span the period 1979–2010, are high-resolution (27 km), and incorporate snow-drift physics that greatly improve the fit of simulated mass balance to around 750 *in situ* measurements (compared to models that ignore snow drifting). By capturing the erosional as well as the sublimation effects of wind, the model⁴¹ is able to compute both surface accumulation and the location and extent of ablation areas. Annual mass balance across the continent is calculated to be $2,418 \pm 181 \text{ Gt}$ per year with only minor interannual variability but a pronounced, winter-dominated, seasonal cycle.

Antarctic surface air temperatures derived from Advanced Very High Resolution Radiometer (AVHRR) infrared data⁴² and updated for the period 1982–2004 (ref. 43) provide high-resolution (6.25 km) continent-wide coverage. Since temperatures are more easily and reliably mapped than surface accumulation, these data^{42,43} are commonly used in ice-sheet modelling.

Oceanic temperatures are harder to measure, and for our experiments we use outputs from an established regional-scale climate model. This model (RegCM3) is coupled with the GENESIS version 3.0 Global Climate Model and is implemented at 80-km resolution^{44,45}. The model includes parameterizations of surface, boundary layer and most processes that account for the physical exchanges between the land surface boundary layer and free atmosphere. It includes detailed representations of snow and near-surface land ice and has been validated against modern observed polar climates and ice-sheet mass balances⁴⁴. Oceanic outputs from this model capture the continental-scale pattern of Antarctic sea surface temperatures but probably underestimate temperatures in areas where recent subsurface warming has been most rapid, such as the inner Amundsen Sea. The underestimation of modern ocean temperatures in this area may be the primary reason that our simulations do not appear to show rapid grounding-line retreat into the Pine Island and Thwaites Glacier subglacial basins, as has been predicted by some models¹⁶, but we also note that the muted and lagged response we see in the Amundsen Sea sector is consistent with the findings of another study⁴⁶.

Since our primary interest lies in continental-scale interpretations, and since our methodology is based on the analysis of deviations from initial conditions (that is, results are bias-corrected), we argue that if any local inaccuracies in our input fields exist they should not substantially affect our conclusions at the continental scale; however, we acknowledge this as an area where future refinements could be made.

Future climate trajectories. To perturb our initial conditions along the trajectories forecast for coming centuries, we use Climate Model Intercomparison Project phase 5 (CMIP5) data for the four RCPs of the Fifth Assessment Report of the Intergovernmental Panel on Climate Change³. We extracted Antarctic-specific (60°–90° S) zonally averaged timeseries of air temperature (ΔT_{air}), effective precipitation (ΔP_{eff}) and sea surface temperature (ΔSST) from the ensemble mean data set for the period 1890–2100 CE (Extended Data Fig. 1 and Extended Data Table 1). Because we use the ensemble mean, rather than the full suite of climate model projections presented in the Fifth Assessment Report of the Intergovernmental Panel on Climate Change³, our simulations do not capture the full range of possible responses implied by the spread of climate model predictions. However, our aim is to present representative outputs that allow first-order differences between the main scenarios to be identified.

Raw data were uniformly adjusted so that perturbations are relative to the present, to ensure consistency with our initial-condition data sets (above). This adjustment effectively results in air temperatures at 1890 CE approximately 0.6 °C below those of the present³. For each of the RCPs, we used the extracted Antarctic-specific air temperature, precipitation and ocean temperature anomalies to update the environmental boundary conditions of our ice-sheet model incrementally throughout the simulations. To extend the CMIP5 RCP values beyond 2100 CE we used long-term trajectories based on the Fifth Assessment Report of the Intergovernmental Panel on Climate Change^{3,47}. In these Extended Concentration Pathway scenarios, all emissions trajectories result in maximum atmospheric temperature perturbations by 2300 CE, and remain unchanged for the remainder of the simulation period (to 5000 CE)^{1,3,47} (Extended Data Fig. 2). In all of our experiments, the magnitudes of precipitation and ocean temperature changes are scaled to air temperature changes according to their respective variance in the zonally averaged CMIP5 data. These indicate that a 1 °C increase in air temperature accounts for a 5.3% increase in precipitation, in agreement with long-term records⁴⁸, whereas ocean temperature changes are approximately one-quarter of that seen in the atmosphere (Extended Data Fig. 1).

In chapter 12 of the Fifth Assessment Report of the Intergovernmental Panel on Climate Change³, long-term (beyond 2300 CE) climate change projections are considered in terms of two scenarios: first, a situation in which atmospheric CO₂ remains constant at 2300 CE levels, and second, where atmospheric CO₂ declines steadily from 2300 CE to 3000 CE. This second scenario, however, results in only a modest reduction in surface air temperatures, and is based on reduction of emissions to zero by 2300 CE. The likelihood of such aggressive mitigation is not

known, but the available data appear to "...support the conclusion that temperatures would decrease only very slowly (if at all), even from strong reductions or complete elimination of CO₂ emissions..." (page 1104 of ref. 3). On this basis, we propagate our environmental forcings beyond 2300 CE at their 2300 CE perturbed level. In most cases this is their maximum, although in RCP 2.6 maxima are reached by 2100 CE, after which they decline.

Code availability. The Parallel Ice Sheet Model is freely available as open-source code from the PISM github repository (<https://github.com/pism/pism>). RegCM3 is available from <https://users.ictp.it/RegCNET/model.html>. CMIP5 data were downloaded from <http://climexp.knmi.nl/>. Bedrock topography and ice thickness data are from the BEDMAP2 compilation, available at <http://www.antarctica.ac.uk/basresearch/ourresearch/az/bedmap2/>. Information on surface mass balance data is available at <http://www.projects.science.uu.nl/iceclimate/models/antarctica.php#racmo21>. Air temperature and geothermal heat flux inputs were taken from the ALBMAP version 1 compilation⁴³ and can be downloaded from <http://doi.pangaea.de/10.1594/PANGAEA.734145>.

Experimental methods. To establish differences in ice-sheet configuration arising under perturbed climate regimes, our initial requirement is for an accurate simulation of the present-day Antarctic ice sheet in which the grounded and floating portions are reproduced in a manner that is as close to observations as possible. Our principal guiding constraints are (1) the volume of grounded ice, (2) grounding-line positions, and (3) the pattern of surface velocities. Building on previous work^{49,50} we implement the following three-stage spin-up procedure in order to produce a thermally equilibrated and dynamically stable simulation of the present-day ice sheet, from which subsequent experiments can be restarted:

(1) Initial 20-year smoothing run in which only the shallow-ice approximation is used to calculate ice flow. This allows the initial ice-sheet surface to relax slightly, removing any anomalies introduced in the initial data collation phase. During this brief run, the calving line is held fixed.

(2) Intermediate 150,000-year run in which the ice geometry is held fixed, but the enthalpy field is allowed to evolve. This allows three-dimensional ice temperatures to evolve to equilibrium under the imposed initial climate conditions.

(3) Final 25,000-year run in which full model physics are employed, including both shallow-ice and shallow-shelf approximations for velocity calculations²⁴, viscoelastic bed deformation³⁹, grounding-line migration²⁷ and calving^{37,38}.

During the 25,000-year final part of this spin-up procedure, all model boundaries (calving line, grounding line, upper and lower surfaces) are free to evolve. Consequently, achieving an ice-sheet geometry at the end of the spin-up that is close to the observed present-day configuration requires careful parameterization. Iterative experimentation focused on manually adjusting flow enhancement factors, basal hydrology and basal traction parameters, and calving coefficients. For each experiment ice thickness and surface velocities were compared to observation-based data to gauge the degree of fit. Because we do not use inverse or iterative methods⁵¹ our fit to present-day constraints has outliers (Extended Data Fig. 3). However, the positions of grounding lines and calving lines are well captured, and the sea-level-equivalent ice volume is within 4% of empirically calculated values⁵². By allowing our tuning experiments to evolve over such long timescales we ensure both that our results are not influenced by transient behaviours and also that our parameterization is robust for multi-millennial integrations. This is essential, since to identify climate-forced perturbations in our study, model drift from incorrect parameterization needs to be minimized.

From the optimal parameterization spin-up run we obtain a thermally equilibrated and dynamically stable present-day ice-sheet simulation that closely resembles the modern ice sheet (Extended Data Fig. 3). This simulation is the starting point for all of the RCP-based experiments. We then run a two-component experimental ensemble in which each of the environmental parameters (air temperature T_{air} , precipitation P_{eff} , ocean temperature SST) evolves according to the rates and magnitudes indicated in the extended CMIP5 ensemble mean trends as described above. One component of our experimentation involves 10-km-resolution runs using the full RCP forcing scenarios. The other component uses 20-km-resolution runs to explore glaciological changes that occur in response to theoretical environmental perturbations. Each of the experiments runs for 5,000 years, starting at year zero with climate and ocean forcings applied in calendar years through to 5000 CE. To minimize the possibility of any transient effects arising during the start-up procedure, environmental boundary conditions are held constant for the first 2,000 years, but all model boundaries (calving line, grounding line, upper and lower surfaces) are free to evolve. Any transient adjustments of the ice sheet occur during this period. From 2000 CE, timeseries environmental forcings (described above) are imposed and the ice-sheet/ice-shelf system evolves accordingly. In addition to the forcing experiments we run an additional control experiment in which the same 5,000-year run is made, starting from identical initial conditions but with no environmental perturbations applied. This is essential for the identification and quantification of any model drift during

the period of interest of the simulation (2000–5000 CE). Since this drift must arise from processes other than environmental forcing we use this control experiment to bias-correct outputs from all other simulations. Even though all model boundaries are allowed to evolve freely, model drift in our control experiment is near zero during the period of interest for both ice-volume and ice-sheet extent (Extended Data Fig. 4), so we do not consider that the bias-correction affects our results. In fact, we consider the low model drift to be additional confirmation that our parameterization is robust. On this basis we are confident that the response seen in the RCP simulations arises solely as a consequence of the combined influence of the simultaneously applied forcings (Fig. 1).

Grounding-line sensitivity and resolution dependence. A key part of our simulations is the migration of ice-sheet grounding lines in response to applied environmental forcings. In theory, to obtain the most accurate predictions of grounding-line locations a numerical scheme is required that is able to solve the full set of Stokes equations for ice flow on a high-resolution (hundreds to thousands of metres) spatial grid⁵³. For continental-scale simulations, however, such an approach presents large challenges, and therefore various alternative schemes exist^{22,27}. These alternatives attempt to capture the critical aspects of grounding-line behaviour while still remaining tractable over large domains (thousands of square kilometres) and long (multi-millennial) model integrations. Of primary concern is whether the grid size over which the scheme is implemented actually influences the model results. Here we use two new grounding-line components that together allow dynamic grounding-line behaviour even with our relatively coarse (10 km) grid, but which may also be regarded as sources of uncertainty in our future ice-volume projections.

The first component is a sub-grid grounding-line scheme²⁷ that interpolates basal shear stress (and, optionally, basal melt fields) at the grounding line in order to facilitate the smoother migration of the grounding line. This approach attempts to capture the effects of lateral contact between ice and ocean as well as the effects of water intrusion beneath the ice sheet. Furthermore, it is logical that a retreating grounding line must be provided with an (oceanic) basal melt value at the sub-grid cell into which it migrates, rather than a basal melt value typical of the grounded ice that characterizes the uninterpolated cell. Whether or not the grounding line would migrate without this interpolation, however, remains a source of uncertainty. Thus in our simulations we present both 'high-' and 'low'-scenario estimates of sea-level-equivalent ice loss based on turning on or off the sub-grid melt interpolation. In other studies that use this scheme⁴⁶, some evidence of resolution dependency is apparent, but whether this is a consequence of the sub-grid scheme or of some other aspect of the model implementation is not clear.

The second component of the grounding-line scheme we adopt is an heuristic scheme that reduces basal traction in the first cell upstream of the grounding line. Smoothing the basal friction gradient across the grounding line should reduce the grid-dependency problems seen in artificial scenarios such as MISMIP3d^{27,54} that invoke large changes in basal traction between grounded and floating domains. However, smoothing the basal friction gradient at the grounding line may make this critical boundary more sensitive to environmental perturbations than in models where basal traction changes abruptly, and thus this also perhaps introduces an element of uncertainty in our ice-volume projections.

Grounding lines are poorly observed in nature due to their inaccessibility, yet ice-shelf basal melt rates typically reach their maxima close to the grounding line, and may be as high as 100 m per year (ref. 55). These rates are, however, highly variable and thus while small environmental perturbations could result in relatively large ice-sheet responses in some areas, the consequences in other sectors could be more muted. Acknowledging these uncertainties, we ran a series of experiments at 10-km resolution in an attempt to quantify (at the continental scale and at the multi-millennial scale) the effects of removing individual aspects of the grounding-line scheme. Extended Data Fig. 6a illustrates sea-level-equivalent volume changes for each of these experiments, in which all other parameters were held constant. Using the sub-grid scheme without the basal traction scheme (green line in Extended Data Fig. 6a) results in a relatively minor change to ice volume compared to the RCP 8.5 simulation that uses the full grounding-line scheme (blue line), whereas using the basal traction scheme without the sub-grid scheme (purple line) results in a much less dynamic ice margin that responds less to applied environmental forcings. Using the basal traction scheme together with the sub-grid scheme in which basal melt is not interpolated produces an intermediate result (grey line). Extended Data Fig. 6e–g illustrates the effect of this change in terms of grounding-line migration through time. If neither the sub-grid nor basal traction schemes are used, the simulated ice sheet not only increases in volume above present-day values, but also becomes less responsive to the applied forcings (orange line).

This sub-grid grounding-line scheme is clearly important, and has been shown to greatly improve the accuracy of grounding-line migrations compared to earlier PISM releases⁵⁴, but its implementation may still result in a certain amount of

resolution dependence under certain circumstances^{27,46}. To assess the uncertainties that may arise from grid resolution alone, we implemented a series of experiments in which we employed identical parameterizations (including sub-grid melt interpolation) except for the horizontal grid spacing used to solve prognostic equations. Extended Data Fig. 6b and c illustrates the convergence of results that occurs when the grid is progressively refined from 80 km to 5 km. The finest of these runs (5 km) was conducted only to 3100 CE, owing to the large computational overhead. In terms of final sea-level-equivalent ice volumes, there is a greater difference between the 40-km and 80-km runs than there is between the 20-km and 40-km runs, and there is no difference at all between the final state of the 10-km and 20-km simulations. At even finer grids, the overall trajectories of ice-volume and grounded-ice area at 10 km resolution agree closely with those of the first three millennia of the 5-km-resolution simulation. The spatial variability that arises at these different resolutions is illustrated in Extended Data Fig. 6d for the 2500 CE time slice, identifying that the greatest resolution-dependent uncertainty appears to occur in the Siple Coast region of West Antarctica, but even in this area there is little difference between the 10-km and 5-km results after 500 years of environmental forcing.

Although the 10-km and 20-km simulations converge on identical final ice volumes, the coarser of these two experiments actually simulates slightly greater ice loss, because it deviates from the ‘control’ ice volume of our simulated present-day ice sheet by approximately +0.5 m sea-level equivalent. To see whether this offset could be reduced, we ran 20 new experiments that explored a range of stress balance parameterizations. We found that by making minor adjustments to both the shallow-ice and shallow-shelf flow enhancement factors (Extended Data Table 2), fully dynamic simulations of the present-day ice sheet could be produced (at either resolution) that are freely evolving over multi-millennial timescales but exhibit minimal model drift and fit equally well to present-day geometric and dynamic constraints at the continental scale. Although these parameterizations were tuned only to reproduce the geometry and dynamics of the present-day ice sheet, we found that similar patterns and rates of grounding-line migration were simulated under RCP forcing scenarios (Extended Data Fig. 6h–j).

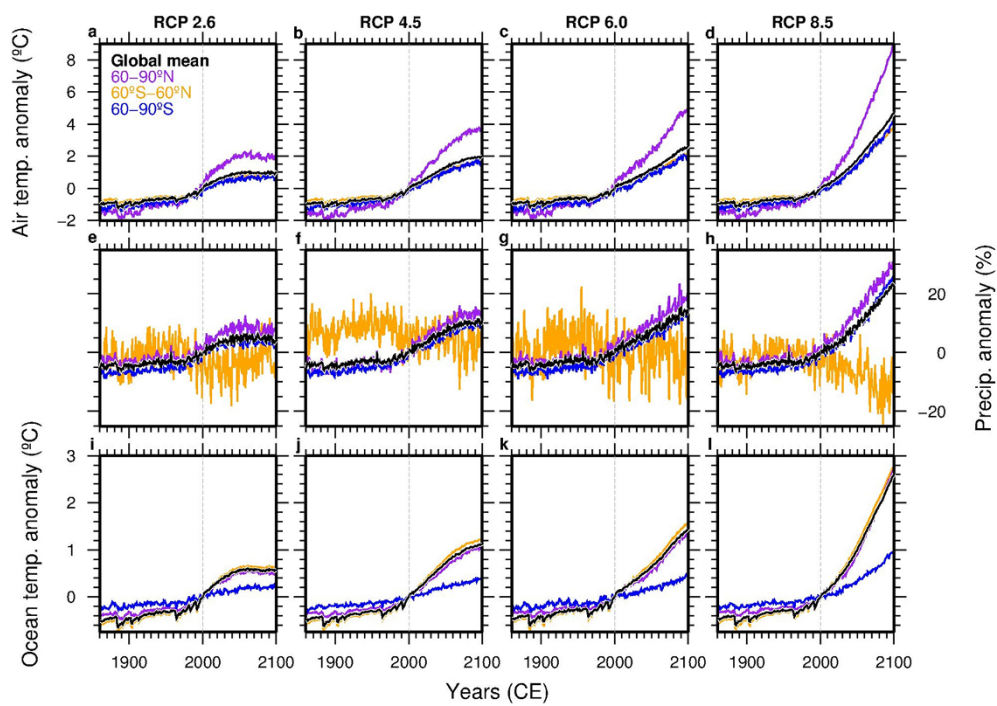
Together, the suite of sensitivity experiments described above illustrate that grounding-line treatment can strongly influence predictions of both the rate of ice-sheet retreat, and the total volume lost for any given forcing. Although the sub-grid melt interpolation scheme still requires physical verification, and tends to favour grounding-line retreat, values from our ‘high’ simulations may still underestimate ice-sheet responses that arise from retreat mechanisms or systemic feedbacks not included in our model. Likewise, the more conventional implementation of sub-grid grounding-line scheme that neglects interpolated basal melt results in more conservative sea-level contributions in our ‘low’ simulations, but still lower values could be possible if unaccounted-for stabilizing mechanisms come into play. Given that geological reconstructions tend to indicate a relatively high ice-sheet sensitivity to warmer climates of the past^{3,56}, we find no compelling reason to favour the conventional grounding-line implementation over the one that includes interpolated basal melt. Regardless of the absolute magnitudes, however, our simulations consistently identify a three-stage response to environmental warming: an initial loss or reduction in ice-shelf area, a dynamic response of grounded ice, and a long-term commitment to sea-level rise that continues for centuries to millennia beyond the initial forcing period.

Polar amplification and long-term equilibrium response. Although there exists some uncertainty as to the form of the RCP projections, particularly beyond 2300 CE, in our experiments we are concerned with the range of likely responses to a plausible range of environmental forcings, and as such we are confident that our ensemble approach captures the likely breadth of Antarctic ice sheet response. Palaeoclimate data and models indicate that, over millennial timescales, polar amplification processes can lead to surface air temperatures, and ocean temperatures, that may be as much as double the magnitude of the global mean perturbation^{56–58}. If this is the case, then our RCP-based experiments represent a conservative lower estimate of the likely ice-sheet response. Furthermore, because we do not use a coupled climate model in our simulations, we cannot fully capture elevation-dependent mass-balance feedbacks that might take place as the ice-sheet geometry evolves. Although we use an elevation-dependent lapse rate to modify air temperatures through the run, it is also likely that, where ice shelves and grounded ice in marine basins are greatly reduced in extent, circulation changes will arise that may bring warmer and wetter air masses further into East Antarctica. To assess the likely implications of even greater warming of the southern high latitudes, we therefore ran duplicate experiments of the RCP 8.5 scenario, with and without sub-grid melt interpolation, and allowed air and ocean temperature anomalies to double by 2300 CE, compared to the original RCP 8.5 experiment. This yields surface air and ocean temperature anomaly maxima of 16 °C and 4 °C respectively, by 2300 CE and beyond. The consequence of this extreme

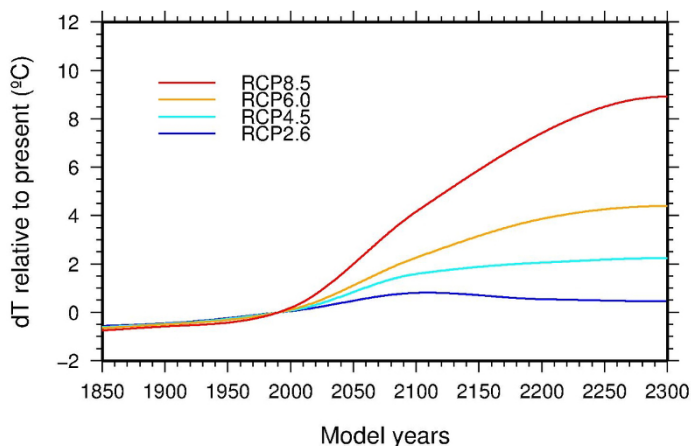
scenario compared to the original RCP 8.5 scenario is illustrated in Extended Data Figs 7 and 8.

We note that although the ice-sheet geometry is visually similar between RCP 8.5 and RCP 8.5A for the ‘high’ scenario (blue outline), the sea-level contribution is 2.1 m greater by 5000 CE under a polar-amplified climate, and the ongoing rate of ice mass loss is 80% higher (Extended Data Fig. 7a, b). In the ‘low’ experiments the difference in sea-level contribution is much greater, with the loss of the WAIS and a considerably higher sea-level contribution arising with amplified warming (8.57 m compared to 5.2 m). With polar amplification, grounding-line retreat into Wilkes Basin occurs under both ‘high’ and ‘low’ scenarios (Extended Data Fig. 7b, c). Extending the simulation to 50,000 years (Extended Data Fig. 7c, d) the full extent of the warming-based commitment under the ‘high’ scenario is far greater than that reached by 5000 CE (15.73 m sea-level equivalent compared to 11.42 m). Under the ‘low’ scenario the difference is much less (9.68 m compared to 8.57 m).

31. Favier, L. *et al.* Retreat of Pine Island Glacier controlled by marine ice-sheet instability. *Nature Clim. Change* **4**, 117–121 (2014).
32. Cornford, S. *et al.* Century-scale simulations of the response of the West Antarctic Ice Sheet to a warming climate. *Cryosphere* **9**, 1579–1600 (2015).
33. Schoof, C. A variational approach to ice stream flow. *J. Fluid Mech.* **556**, 227–251 (2006).
34. Leguy, G. R., Asay-Davis, X. S. & Lipscomb, W. H. Parameterization of basal friction near grounding lines in a one-dimensional ice sheet model. *Cryosphere* **8**, 1239–1259 (2014).
35. Tsai, V. C., Stewart, A. L. & Thompson, A. F. Marine ice-sheet profiles and stability under Coulomb basal conditions. *J. Glaciol.* **61**, 205–215 (2015).
36. Holland, D. M. & Jenkins, A. Modeling thermodynamic ice-ocean interactions at the base of an ice shelf. *J. Phys. Oceanogr.* **29**, 1787–1800 (1999).
37. Albrecht, T. & Levermann, A. Fracture field for large-scale ice dynamics. *J. Glaciol.* **58**, 165–176 (2012).
38. Levermann, A. *et al.* Kinematic first-order calving law implies potential for abrupt ice-shelf retreat. *Cryosphere* **6**, 273–286 (2012).
39. Bueler, E. D., Lingle, C. S. & Brown, J. Fast computation of a viscoelastic deformable Earth model for ice-sheet simulations. *Ann. Glaciol.* **46**, 97–105 (2007).
40. Gomez, N., Pollard, D., Mitrovica, J. X., Huybers, P. & Clark, P. U. Evolution of a coupled marine ice sheet-sea level model. *J. Geophys. Res.* **117**, F01013 (2012).
41. Lenaerts, J., van den Broeke, M., van de Berg, W., van Meijgaard, E. & Munneke, P. A new, high-resolution surface mass balance map of Antarctica (1979–2010) based on regional atmospheric climate modeling. *Geophys. Res. Lett.* **39**, L04501 (2012).
42. Comiso, J. Variability and trends in Antarctic surface temperatures from in situ and satellite infra-red measurements. *J. Clim.* **13**, 1674–1696 (2000).
43. Le Brocq, A., Payne, A. & Vieli, A. An improved Antarctic dataset for high resolution numerical ice sheet models (ALBMAP v1). *Earth Syst. Sci. Data* **2**, 247–260 (2010).
44. Thompson, S. L. & Pollard, D. Greenland and Antarctic mass balances for present and doubled atmospheric CO₂ from the genesis version-2 global climate model. *J. Clim.* **10**, 871–900 (1997).
45. Pal, J. S. *et al.* Regional climate modeling for the developing world: the ICTP RegCM3 and RegCNET. *Bull. Am. Meteorol. Soc.* **88**, 1395–1409 (2007).
46. Martin, M. A., Levermann, A. & Winkelmann, R. Comparing ice discharge through West Antarctic Gateways: Weddell vs. Amundsen Sea warming. *Cryosphere Discuss.* **9**, 1705–1733 (2015).
47. Zickfeld, K. *et al.* Long-term climate change commitment and reversibility: an EMIC intercomparison. *J. Clim.* **26**, 5782–5809 (2013).
48. Frieler, K. *et al.* Consistent evidence of increasing Antarctic accumulation with warming. *Nature Clim. Change* **5**, 348–352 (2015).
49. Golledge, N. R., Fogwill, C. J., Mackintosh, A. N. & Buckley, K. M. Dynamics of the Last Glacial Maximum Antarctic ice-sheet and its response to ocean forcing. *Proc. Natl. Acad. Sci. USA* **109**, 16052–16056 (2012).
50. Golledge, N. *et al.* Antarctic contribution to meltwater pulse 1A from reduced Southern Ocean overturning. *Nature Commun.* **5**, 1–10 (2014).
51. Pollard, D. & DeConto, R. M. A simple inverse method for the distribution of basal sliding coefficients under ice sheets, applied to Antarctica. *Cryosphere* **6**, 953–971 (2012).
52. Fretwell, P. *et al.* Bedmap2: improved ice bed, surface and thickness datasets for Antarctica. *Cryosphere* **7**, 375–393 (2013).
53. Durand, G., Gagliardini, O., Zwinger, T., Le Meur, E. & Hindmarsh, R. C. Full Stokes modeling of marine ice sheets: influence of the grid size. *Ann. Glaciol.* **50**, 109–114 (2009).
54. Pattyn, F. *et al.* Grounding-line migration in plan-view marine ice-sheet models: results of the ice2sea MISMIP3d intercomparison. *J. Glaciol.* **59**, 410–422 (2013).
55. Dutrieux, P. *et al.* Pine Island glacier ice shelf melt distributed at kilometre scales. *Cryosphere* **7**, 1543–1555 (2013).
56. Naish, T. & Zwartz, D. Palaeoclimate: looking back to the future. *Nature Clim. Change* **2**, 317–318 (2012).
57. Graversen, R. G. & Wang, M. Polar amplification in a coupled climate model with locked albedo. *Clim. Dyn.* **33**, 629–643 (2009).
58. Masson-Delmotte, V. *et al.* in *Climate Change 2013: The Physical Science Basis. Contribution of Working Group I to the Fifth Assessment Report of the Intergovernmental Panel on Climate Change* (eds Stocker, T. *et al.*) 383–464 (2013).
59. Rignot, E., Mouginot, J. & Scheuchl, B. Ice flow of the Antarctic Ice Sheet. *Science* **333**, 1427–1430 (2011).

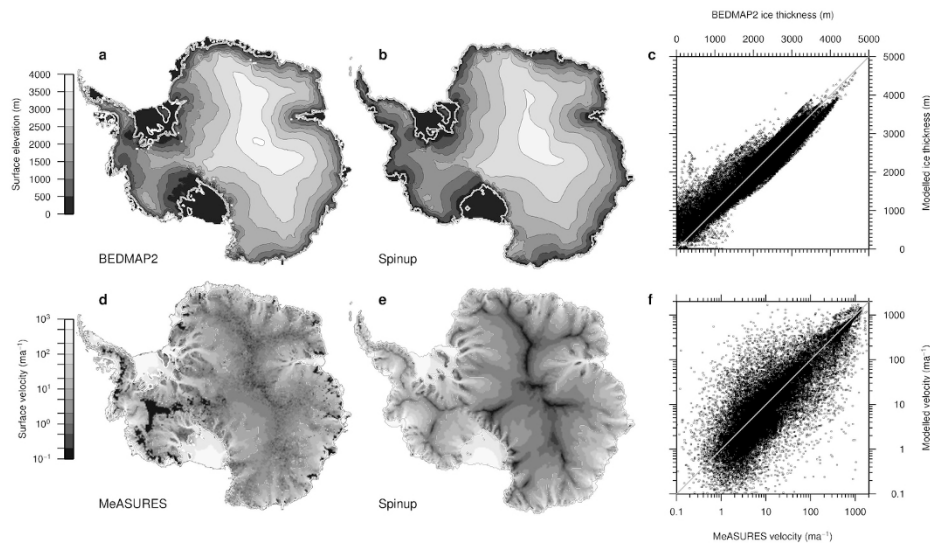


Extended Data Figure 1 | CMIP5 multi-model ensemble mean anomaly timeseries data. Air temperature (a-d), precipitation (e-h) and ocean temperature (i-l) changes for four RCP scenarios expressed as perturbations from present, both for hemispheric sectors and for the global mean.

**Extended Data Figure 2 | Long-term RCP temperature scenarios.**

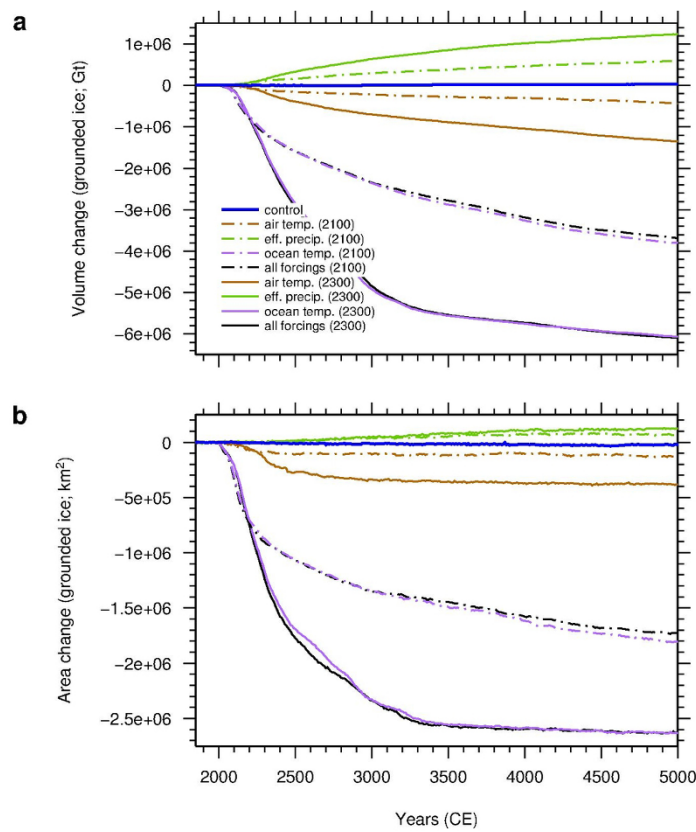
Antarctic-specific (60° – 90° S) projected temperature trends to 2300 CE based on CMIP5 values at 2100 CE and extended to 2300 CE following trajectories of global means from intermediate-complexity Earth system models^{3,47}. Precipitation and ocean temperature trends are calculated to follow those of

atmospheric temperatures, with magnitudes based on analysis of the CMIP5 data set indicating a 5.3% increase in precipitation per degree air temperature increase and a ratio of 0.25 for converting atmospheric to oceanic temperature changes. dT , change in air temperature.



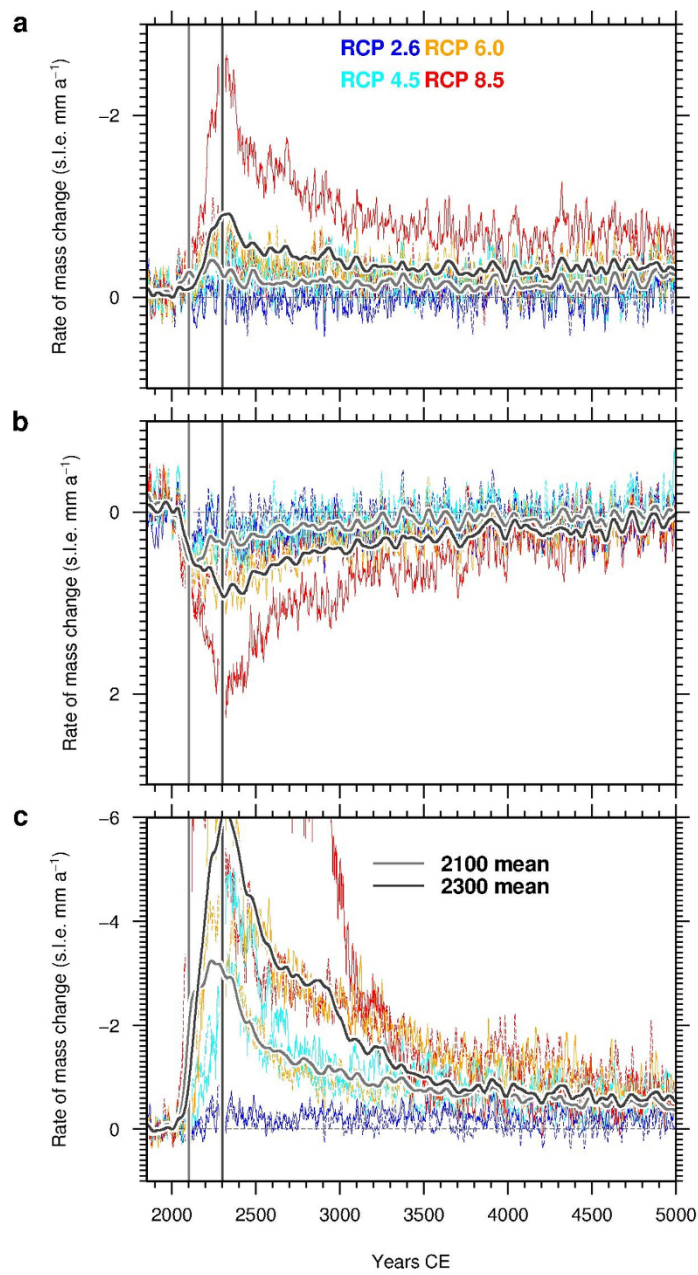
Extended Data Figure 3 | Model spin-up and fit to present-day. Ice-sheet geometry and surface velocities (m a^{-1} , metres per year) at the end of a 25,000-year evolutionary simulation. **a** and **b**, Observation-based⁵² (**a**) and modelled (**b**) ice-sheet extent and surface elevations. **c**, Comparison of ice

thicknesses shown in **a** and **b**. **d** and **e**, Measured⁵⁹ (**d**) and modelled (**e**) surface ice velocities. **f**, Comparison of the ice velocities shown in **d** and **e**. 'MeASURES' is the name of the published ice velocity dataset of ref. 59.



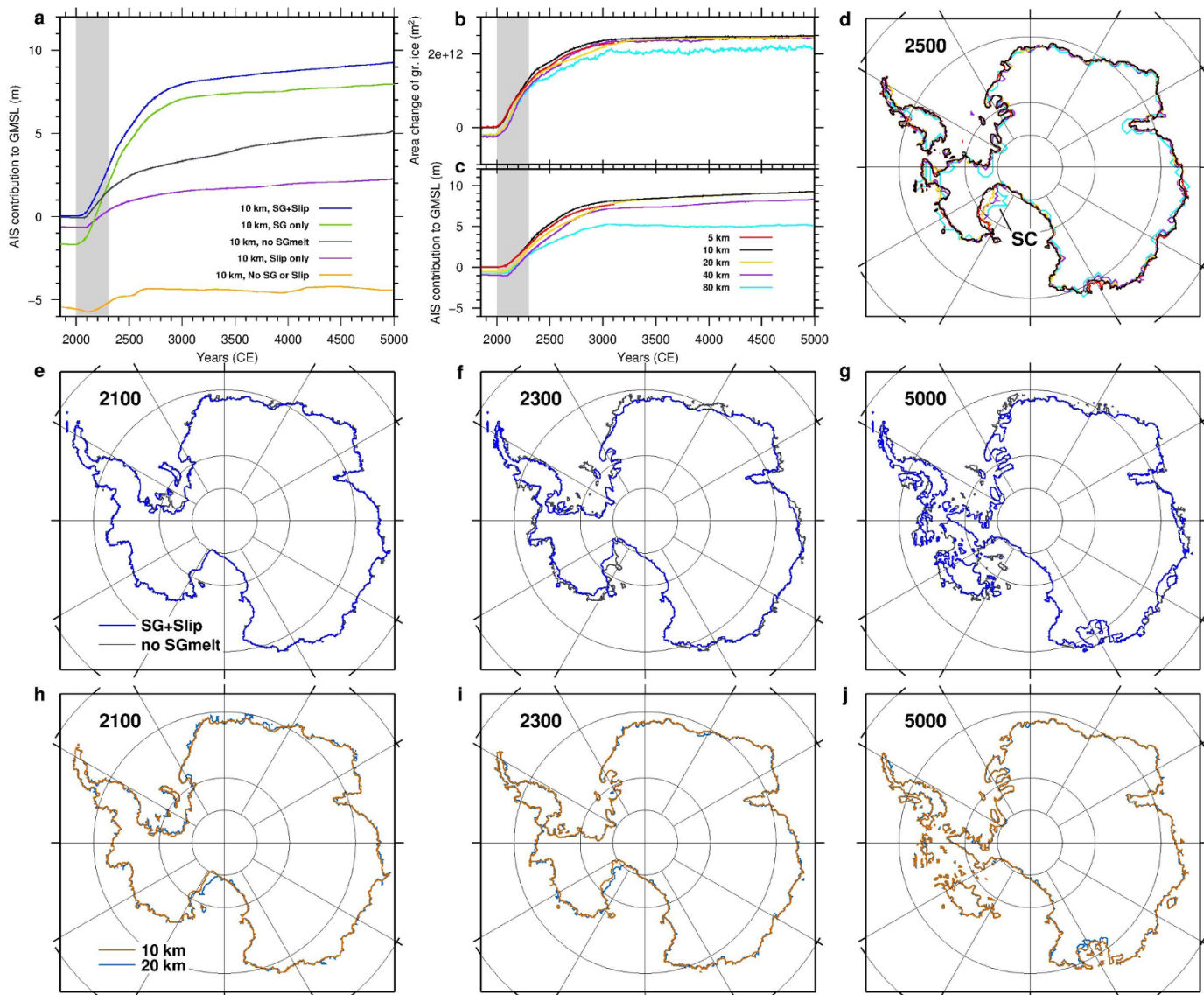
Extended Data Figure 4 | Multi-millennial changes in ice-sheet volume and area. Simulated changes in ice-sheet volume (a) and ice-sheet area (b) under single-parameter and combined forcings (ΔT_{air} , ΔP_{eff} and ΔSST), based on

simplified RCP scenarios for 100-year and 300-year forcing periods. Also shown in both panels is the control experiment (thick blue lines), illustrating little to no drift during the period of interest to 5000 CE.



Extended Data Figure 5 | Multi-millennial changes in ice-sheet response to single-parameter environmental forcings. Bias-corrected rates of sea-level-equivalent ice-mass change (s.l.e. mm a⁻¹, millimetres of sea level equivalent per year) for each of the single-parameter simplified RCP forcing experiments. **a**, Rates of change under applied air temperature forcings peak at around 2240–2330 CE for both the 100-year and 300-year forcing experiments and decline thereafter, but both the 100-year and 300-year experiments exhibit rates that are still much larger than initial values by 5000 CE. **b**, Ice-mass rates of change as

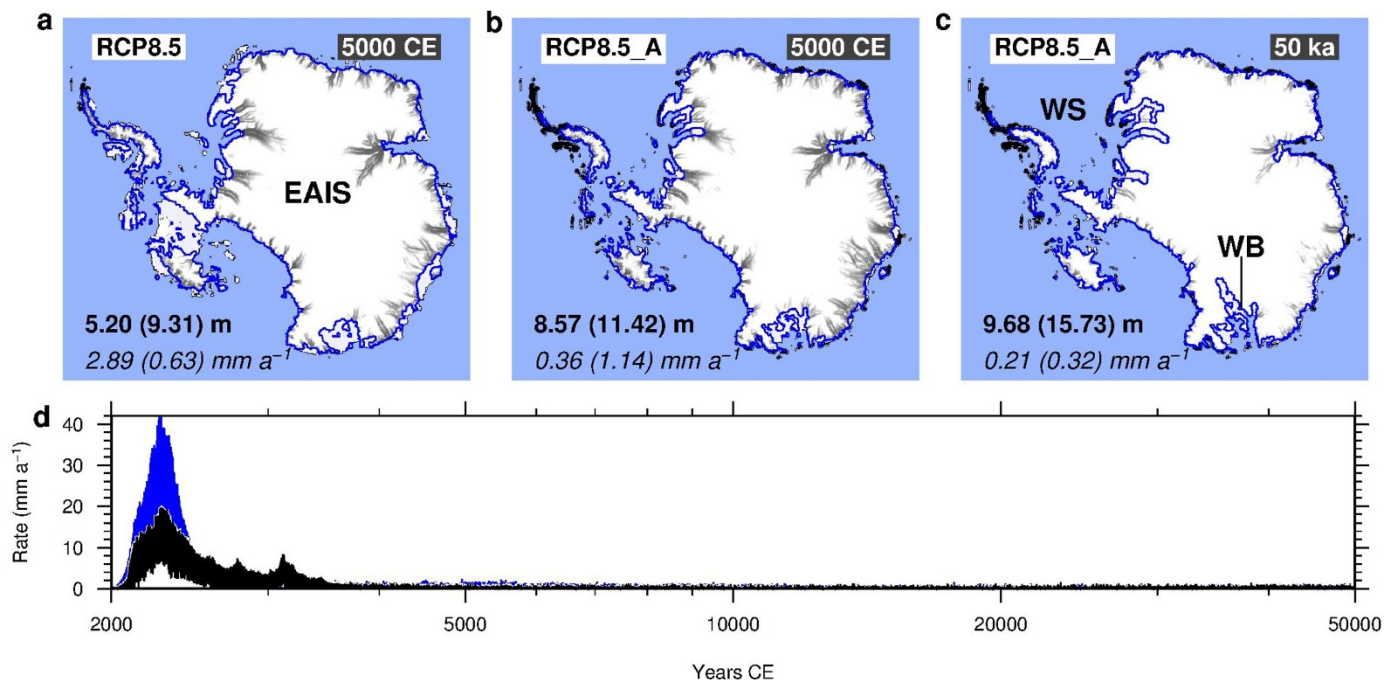
in **a** but forced only with precipitation changes. Maxima for the 100-year and 300-year forcing experiments occur close to the end of the forcing period, reflecting little inherent lag. **c**, Rates of change in response to ocean forcing show much more elevated initial peaks compared to mass-loss rates in subsequent millennia. By the end of the run, rates of mass loss for both the 100-year and 300-year forcing experiments are still higher than at the beginning of the run. Data are shown relative to zero at 2000 CE.



Extended Data Figure 6 | Model sensitivity and uncertainties. **a**, Modelled ice volume changes relative to the control run (in sea-level equivalent) for simulations in which only the grounding-line parameterization is altered. 'SG' and 'Slip' denote respectively the sub-grid and reduced traction grounding-line schemes employed in our simulations; 'no SGmelt' indicates an experiment in which only the sub-grid basal melt interpolation scheme is turned off (see Methods for details). Grey shading denotes period of applied forcing. **b** and **c**, Domain-integrated grounded (gr.) ice area (**b**) and sea-level-equivalent ice volume (**c**) trajectories under RCP 8.5 conditions for simulations in which the full sub-grid scheme is used and only the model resolution is changed. The 5-km simulation was not run beyond 3100 CE owing to the large computational

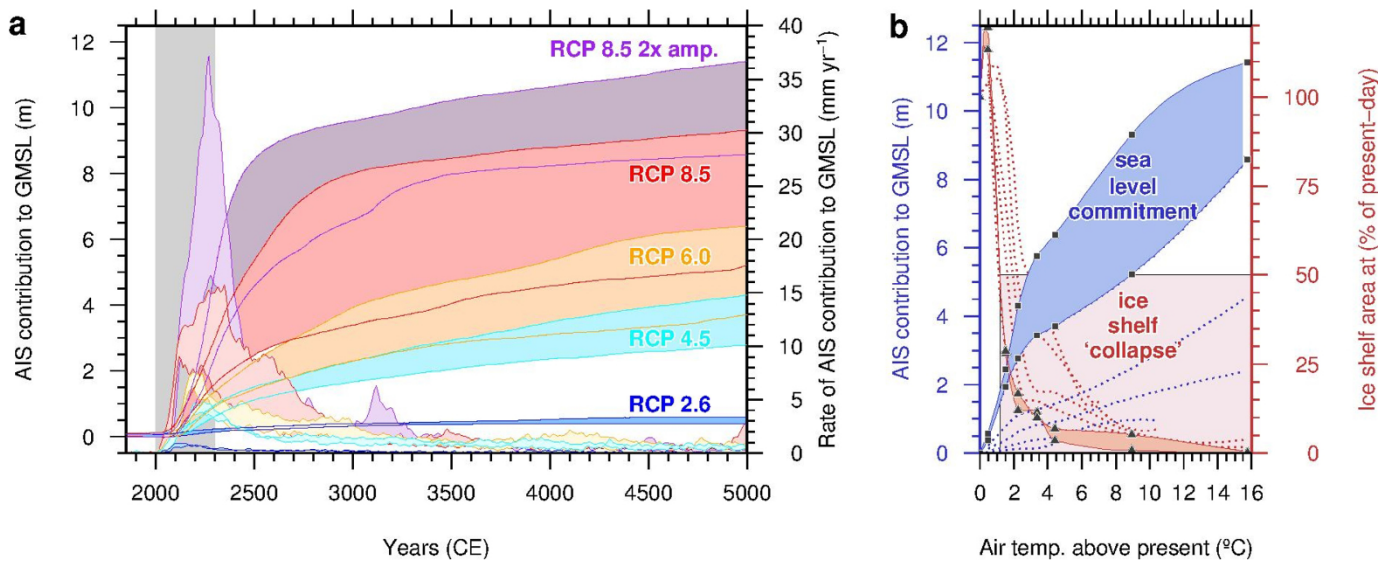
overhead. **d**, Grounding-line positions at 2500 CE for the experiments shown in **b** and **c**. The greatest differences occur in the Siple Coast area (SC). Note the very close agreement between the 10-km and 5-km simulations.

e-g, Grounding-line locations under RCP 8.5 conditions at 2100 CE (**e**), 2300 CE (**f**) and 5000 CE (**g**) for experiments using the full grounding-line parameterization ('SG+Slip') compared to those in which the sub-grid basal melt interpolation is turned off ('no SGmelt'). **h-j**, Grounding-line locations under RCP 8.5 conditions at 2100 CE (**h**), 2300 CE (**i**) and 5000 CE (**j**) for 10-km and 20-km simulations that use the full grounding-line parameterization and resolution-specific stress balance tunings.



Extended Data Figure 7 | The effect of polar amplification. **a**, Geometry of the modelled Antarctic ice sheets under RCP 8.5 at 5000 CE, using both variants of the grounding-line scheme. Bold values and those in italics denote magnitudes and rates of sea-level contributions respectively. Leading values and those in parentheses relate to 'low' and 'high' scenarios respectively. Panels show ice extent for 'low' simulations; blue lines show grounding-line locations for 'high' simulations. Pale blue shading shows grounded ice lost in 'high' simulations but present in the 'low' scenario. **b**, Duplicate simulation to **a** but using a 2 × amplification of Antarctic temperatures beyond 2300 CE. Note the

greater sea-level contribution compared to **a**. **c**, The full equilibrium response of the polar amplification scenario shown in **b**. Note the greater loss of ice from the Wilkes Basin (WB) and eastern Weddell Sea (WS), resulting in a higher total sea-level contribution. Black areas denote ice-free land. **d**, Rate of ice loss for the 2 × amplification scenario for 'low' (black) and 'high' (blue) scenarios, illustrating that although the fastest contribution to sea level (2–4 m per century) occurs during the first millennium, slower mass loss continues for many millennia thereafter.



Extended Data Figure 8 | Antarctic contribution to GMSL. **a**, Predicted sea-level contribution from the AIS for ‘high’ and ‘low’ simulations (coloured lines) under each of the four RCP scenarios as well as one that includes $2 \times$ amplification of Antarctic temperatures by 2300 CE (darker shading), based on coeval climatic and oceanic perturbations. The forced response (grey shading) represents 20% to 42% of the committed response by 5000 CE. Lighter shading between coloured lines shows rates of sea-level-equivalent ice loss for each scenario. **b**, Long-term sea-level commitment as a function of atmospheric warming (blue shading with squares). Intermediate response

curves for the ‘low’ simulations are shown in dotted lines. Red shading with triangles shows relationship between ice-shelf area and atmospheric warming for the near-equilibrium response and for intermediate stages (dotted lines). All curves in **b** are based on data from the four RCP scenario simulations, as well as one that includes $2 \times$ amplification of Antarctic temperatures by 2300 CE, and two additional experiments whose maximum air temperature forcings are 1.5°C and 3.35°C . Pink shading defines the temperature range within which an ice-shelf extent less than 50% of present is simulated.

Extended Data Table 1 | CMIP5 multi-model ensemble mean environmental perturbations

| | | RCP 2.6 | RCP 4.5 | RCP 6.0 | RCP 8.5 |
|-----------------------------|-----------|---------|---------|---------|---------|
| air temp. anomaly (°C) | Global | 0.9 | 2.0 | 2.6 | 4.7 |
| | Antarctic | 0.8 | 1.6 | 2.3 | 4.2 |
| precip. anomaly (%) | Global | 4.2 | 10.9 | 13.2 | 22.6 |
| | Antarctic | 4.0 | 9.4 | 13.4 | 24.5 |
| ocean temp. anomaly (°C) | Global | 0.6 | 1.1 | 1.4 | 2.6 |
| | Antarctic | 0.2 | 0.4 | 0.5 | 1.0 |

Air temperature, precipitation and ocean temperature changes (ΔT_{air} , ΔP_{eff} and ΔSST) by 2100 for each of the RCP scenarios, expressed as perturbations from present.

Extended Data Table 2 | Parameter values found to best reproduce present-day Antarctic ice-sheet configuration

| Parameter | Value | Units |
|---------------------------------|--------------------|--------------------|
| Domain resolution (x, y) | 20 or 10 | km |
| Ice grid resolution (z) | 0.024 | km |
| Bedrock grid resolution (z) | 0.1 | km |
| Air temperature lapse rate | -0.008 | °C m ⁻¹ |
| SIA enhancement | 1.2 or 1.47 | - |
| SSA enhancement | 0.5 or 0.57 | - |
| Till porewater fraction | 0.8 | - |
| Eigen calving coefficient | 5e+17 | - |
| Thickness calving limit | 220 | m |
| Density of lithosphere | 3300 | kg m ⁻³ |
| Flexural rigidity | 5×10^{24} | Nm |
| Viscosity of mantle | 1×10^{19} | Pa s |

Note that different values of enhancement of shallow-ice and shallow-shelf approximations (SIA and SSA) are used for the 10-km- and 20-km-resolution simulations.